

## Quantitative analysis of the vertical-averaging approximation for evaporating thin liquid films

Christopher Larsson  and Satish Kumar <sup>\*</sup>

*Department of Chemical Engineering and Materials Science, University of Minnesota, Minneapolis, Minnesota 55455, USA*



(Received 21 October 2021; accepted 9 August 2022; published 12 September 2022)

Thin liquid films play a central role in coating processes and other industrial and natural applications. Efficient optimization of these processes requires an understanding of capillary leveling, Marangoni flow, evaporation, and related phenomena. Although mathematical models are useful for gaining such understanding, it can be difficult to extract physical insight as the number of phenomena considered increases, so simplifying assumptions such as the vertical-averaging (VA) approximation for solute concentration are often employed. In this work, we consider two-component films consisting of a solute and volatile solvent and use lubrication theory to examine the performance of the VA approximation for three common evaporation models: constant, one-sided, and diffusion-limited. Whereas the VA approximation typically assumes  $\epsilon^2\text{Pe} \ll 1$ , where  $\epsilon$  is the aspect ratio and  $\text{Pe}$  is the Péclet number, we find that the critical value of  $\epsilon^2\text{Pe}$  beyond which the VA approximation breaks down is often much larger than unity and depends on the evaporation rate. Furthermore, applying the VA approximation outside of its regime of validity results in drastically different film-height and solute-distribution predictions depending on the evaporation model. Scaling relations are derived from physical arguments to show how the critical value of  $\epsilon^2\text{Pe}$  depends on the evaporation rate under each evaporation model.

DOI: [10.1103/PhysRevFluids.7.094002](https://doi.org/10.1103/PhysRevFluids.7.094002)

### I. INTRODUCTION

Thin liquid films play a key role in numerous industrial processes including the application of paint [1–3] and the creation of flexible electronics [4]. Optimization of these processes requires fundamental understanding of film behavior, which is also useful for gaining insight into many natural processes [5–9]. Theoretical models are desirable for developing this understanding because they allow one to systematically explore the influence of various phenomena such as capillary and Marangoni flow, solute transport, and evaporation. However, theoretical models quickly become cumbersome as the number of phenomena considered increases, so it is extremely useful to make well-justified simplifications.

It is often desired that thin liquid films have controlled thicknesses and species distributions so that they exhibit desired functionality. To model species transport in a binary film with a solvent and solute, one usually takes the solute concentration to be governed by a convection-diffusion equation. A general formulation considers solute transport through the film depth as well as across the film width, which significantly increases the computational cost of a numerical solution. However, when solute diffusion is sufficiently rapid, one may approximate vertical diffusion as a quasi-steady-state process and consider only solute transport across the film width. This drastically reduces model complexity and is the basis of the vertical-averaging (VA) approximation introduced by Jensen

---

<sup>\*</sup>Corresponding author: [kumar030@umn.edu](mailto:kumar030@umn.edu)

and Grotberg [10]. However, the formal assumptions underlying this approximation are strict for physical systems and the limits of its validity have not been systematically explored under evaporation [11]. Still, the VA approximation (or assumption of vertical uniformity) is popular due to the simplicity it provides [3,12–19].

For industrial applications, liquid films are often solidified through evaporation, curing, or other mechanisms. With evaporation, solvent evaporates from the film, leaving behind a solute-rich, solidified film. The process of evaporation consists of two main steps. First, solvent molecules escape from the liquid phase into the gas phase (the phase-change step). Second, the gaseous solvent molecules diffuse away from the liquid-air interface (the diffusion step). To include evaporation in a theoretical model, one must use an equation to express evaporative fluxes in terms of known quantities such as the film height and solute concentration.

Evaporation models have been developed in previous work, typically assuming a different portion of the evaporative process is limiting. The one-sided evaporation model assumes evaporation is limited by the phase-change step [20,21], whereas the diffusion-limited model assumes evaporation is limited by the diffusion step. Another common approach is to simply assume evaporation is uniform and constant. As will be discussed below, previous studies on the evolution of evaporating thin films and droplets have employed various combinations of evaporation models and the VA approximation. We will show in Sec. III that the choice of evaporation model, as well as use of the VA approximation, leads to significant qualitative differences in model predictions.

#### A. Constant evaporation

Constant evaporation is a simple, convenient approximation that assumes the evaporation rate is uniform and constant, making it useful for probing fundamental mechanisms. Considering constant evaporation, Serpetsi and Yiantsios [22] examined the stability of a drying binary film and Yiantsios and Higgins [23,24] studied the influence of soluble surfactants and colloidal particles on the evolution of drying films. Yiantsios *et al.* [25] studied the evolution of a drying polymer film, finding strong dependence on the formation of vertical concentration gradients. Because of its simplicity, constant evaporation has also been used in other studies where the problem is already complex due to factors such as the problem geometry or the presence of colloidal particles [4,19,26–28].

#### B. One-sided evaporation

The evolution of drying films and droplets consisting of a pure volatile liquid has been extensively studied under one-sided evaporation [5,6,20,21,29,30]. Pham *et al.* [12] studied the evolution of multicomponent thin films on substrates with topography using this evaporation model. The distribution of colloidal particles in evaporating droplets has also been studied [13,18,31–33]. Many of these studies employ a VA approximation or an assumption of vertical uniformity to ease model complexity. However, Maki and Kumar [32] did not use the VA approximation and were able to capture skin formation (buildup of colloidal particles at the liquid-air interface), which has been shown to inhibit evaporation [34] and significantly affect evolution dynamics [35].

#### C. Diffusion-limited evaporation

Diffusion-limited evaporation is commonly used for evaporating droplets, but has also been used for evaporating films [9,36–38]. Deegan *et al.* [39,40] provided an analytical solution for the evaporative flux of a spherical-cap droplet. Other studies have examined the influence of contact angles [41], species concentration [42,43], and many other important quantities on droplet evolution under diffusion-limited evaporation [14,15,44–46]. To ease computational complexity, many of these studies assumed vertical uniformity of any species in the droplets. However, Diddens *et al.* [42] have demonstrated that vertically nonuniform temperature and solute concentration in binary droplets can have significant effects on droplet evolution. In Sec. III, we will examine the effects of nonuniform solute concentration on diffusion-limited evaporation in thin films.

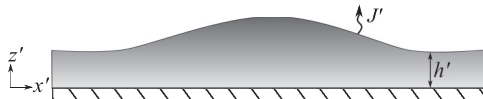


FIG. 1. Schematic of an evaporating film containing a nonvolatile solute. Shading depicts solute buildup at the liquid-air interface due to solvent evaporation.

Previous studies have examined the accuracy of the one-sided and diffusion-limited evaporation models under various experimental conditions, but are largely limited to evaporating droplets. Sotke *et al.* [29] demonstrated excellent agreement between theory and experiment using the one-sided evaporation model for evaporating droplets on heated substrates. Assuming spherical-cap droplets, Deegan *et al.* [40] highlight agreement between theory and experiment using diffusion-limited evaporation. Hu and Larson [41] built on this work, also showing excellent agreement between theory and experiment with diffusion-limited evaporation. Many other studies have reported experimental data regarding evaporation that has found agreement with subsequent theoretical studies using the one-sided or diffusion-limited evaporation models [14,15,37,47,48].

Few studies have directly addressed the differences between the common evaporation models [37,48], and to the best of our knowledge, none have addressed the performance of the VA approximation in the presence of evaporation [11]. The importance of phenomena driven by vertical concentration gradients (and thus the validity of the VA approximation) strongly depends on the rate of diffusion; rapid vertical diffusion will quickly smooth out gradients in species concentration. However, precisely what is considered “rapid” diffusion has not been well established. The VA approximation offers a desirable simplicity, but its influence on the predicted interface shape and species distribution remains unexplored. Therefore, this work presents an analysis of the VA approximation under evaporation for the foundational case of a two-dimensional binary film with volatile solvent and nonvolatile solute. In Sec. II, we derive a two-dimensional (2D) description of the film height and solute concentration in the film which is then simplified using the VA approximation. To focus on solutal Marangoni flow, we neglect any thermal Marangoni flow induced by evaporation of solvent (discussed further in Sec. II D). In Sec. III, we compare results from the 2D description and VA approximation for different evaporation models to gauge the performance of the VA approximation. We then develop scaling relations to gain physical insight into the mechanisms that the VA approximation fails to capture. Conclusions are given in Sec. IV.

## II. MATHEMATICAL MODEL

We seek to model the film height and species concentration in an evaporating binary thin film as depicted in Fig. 1. The liquid consists of a solvent and solute such that solute concentration gradients create Marangoni stresses that drive Marangoni flow, which in turn creates film-height nonuniformities as shown in Fig. 1. Film height  $h'(t', x')$  and solute concentration  $c'(t', x', z')$  vary with time  $t'$  and the spatial variables  $x'$  and  $z'$ . The evaporative solvent mass flux  $J'(t', x')$  is expressed as a function of  $h'$  and  $c'$  through evaporation models. We assume periodic boundary conditions in the  $x'$  direction.

### A. Hydrodynamics

The liquid is assumed Newtonian with constant density  $\rho$  and viscosity  $\mu$ . Surface tension  $\sigma'$  is scaled by the pure solvent surface tension  $\sigma_0$  and solute concentration  $c'$  is scaled by an initial concentration  $c_0$ . It is assumed that the ratio of the vertical and lateral characteristic lengths  $\epsilon = H/L \ll 1$ , allowing the application of lubrication theory. Here,  $H$  is the initial film height and  $L$  is obtained by balancing viscous and Marangoni stresses at the interface:

$$\mu \frac{\sigma_0 H^2}{\mu L^3} \sim \frac{\omega_0 c_0}{L} \frac{\partial \sigma'}{\partial c'} \Rightarrow L \sim \frac{H}{\sqrt{\text{Ma}}}, \quad (1)$$

where  $\omega_0$  is the initial mass/mole fraction of solute. The viscous scale used in this balance is based on a capillary velocity found by considering mass and momentum balances [11]. Relation (1) shows that  $\epsilon \sim \sqrt{\text{Ma}}$ , and thus lubrication theory requires that  $\sqrt{\text{Ma}} \ll 1$ . The Marangoni number  $\text{Ma}$  is the dimensionless change in surface tension with solute concentration,  $\text{Ma} = -(\omega_0 c_0 / \sigma_0) \partial \sigma' / \partial c' |_{c'=0}$ . It is assumed that the solute lowers the surface tension of the liquid so that  $\text{Ma} > 0$ . The case of  $\text{Ma} < 0$  can also occur in practice [12] but is not investigated here for the sake of brevity.

The liquid motion is described by the Navier-Stokes equations supplemented with no-slip and no-penetration conditions at the substrate and stress balances at the liquid-air interface. Pressure  $p'$  is scaled by  $p^* = \sigma_0 \epsilon^2 / H$ ,  $x$ -velocity  $v'_x$  by  $v_x^* = \epsilon^3 \sigma_0 / \mu$ ,  $z$ -velocity  $v'_z$  by  $v_z^* = \epsilon v_x^*$ , and time  $t'$  by  $t^* = H / v_x^* \epsilon$ . These scales are derived by balancing the relevant terms in the mass and momentum balances [11]. Finally, we use the scale  $J^*$  for the evaporative mass flux  $J'$  that will be given in Sec. II C. For the remainder of this work, we use dimensionless variables (indicated without a prime superscript):

$$\begin{aligned} x' &= \epsilon^{-1} H x, & z' &= H z, & h' &= H h, & \sigma' &= \sigma_0 \sigma, & c' &= c_0 c, \\ v'_x &= v_x^* v_x, & v'_z &= \epsilon v_x^* v_z, & p' &= p^* p, & t' &= t^* t, & J' &= J^* J. \end{aligned} \quad (2)$$

The surface tension  $\sigma$  varies linearly with solute concentration  $c$  at the interface  $z = h$ ,

$$\sigma = 1 - \text{Ma} c|_{z=h}. \quad (3)$$

This assumes a dilute solute ( $\omega_0 \ll 1$ ) and has been used in previous studies (e.g., Refs. [12] and [22]). Here we neglect thermal Marangoni flow to focus on solutal Marangoni flow, but we will revisit thermal effects in Sec. II D after deriving expressions for the evaporative flux under each evaporation model. Applying lubrication theory, we retain only leading-order terms in the Navier-Stokes equations to obtain

$$\frac{\partial^2 v_x}{\partial z^2} = \frac{\partial p}{\partial x}, \quad (4)$$

$$\frac{\partial p}{\partial z} = 0, \quad (5)$$

$$\frac{\partial v_x}{\partial x} + \frac{\partial v_z}{\partial z} = 0. \quad (6)$$

No-slip, no-penetration, and stress balance conditions yield the boundary conditions

$$v_x|_{z=0} = v_z|_{z=0} = 0, \quad (7)$$

$$p|_{z=h} = -\frac{\partial^2 h}{\partial x^2}, \quad (8)$$

$$\left. \frac{\partial v_x}{\partial z} \right|_{z=h} = -\frac{\partial c|_{z=h}}{\partial x}. \quad (9)$$

Note that due to the choice of lateral length scale  $L = H / \sqrt{\text{Ma}}$ , the Marangoni number  $\text{Ma}$  does not appear in tangential stress balance (9). Solving these equations for the liquid velocities yields [6]

$$v_x = -\left(\frac{1}{2}z^2 - hz\right) \frac{\partial^3 h}{\partial x^3} - \frac{\partial c|_{z=h}}{\partial x} z, \quad (10)$$

$$v_z = \left(\frac{1}{6}z^3 - \frac{1}{2}hz^2\right) \frac{\partial^4 h}{\partial x^4} + \frac{1}{2} \left(\frac{\partial^2 c|_{z=h}}{\partial x^2} - \frac{\partial h}{\partial x} \frac{\partial^3 h}{\partial x^3}\right) z^2. \quad (11)$$

Mass conservation at the interface  $z = h$  leads to the kinematic condition

$$v_z = \frac{\partial h}{\partial t} + v_x \frac{\partial h}{\partial x} + EJ, \quad (12)$$

where the evaporative number  $E = J^*/\rho v_x^* \epsilon$  (ratio of evaporative flux to convective flux) and mass flux  $J$  arise from solvent evaporation. The definitions of  $J$  and  $J^*$  depend on the evaporation model and are discussed in Sec. II C. Substituting Eqs. (10) and (11) into Eq. (12) yields the thin-film equation

$$\frac{\partial h}{\partial t} = \underbrace{-\frac{1}{3} \frac{\partial}{\partial x} \left[ h^3 \frac{\partial^3 h}{\partial x^3} \right]}_{\text{Capillary Flow}} + \underbrace{\frac{1}{2} \frac{\partial}{\partial x} \left[ h^2 \frac{\partial c|_{z=h}}{\partial x} \right]}_{\text{Marangoni Flow}} - \underbrace{EJ}_{\text{Evaporation}}. \quad (13)$$

Thus, the evolution of film height  $h$  is coupled to that of solute concentration  $c$  through Marangoni flow and evaporation.

## B. Solute concentration

The VA approximation simplifies the convection-diffusion equation under the assumption of rapid vertical diffusion. We begin by deriving a 2D description that does not employ the VA approximation in Sec. II B 1 and then give a derivation of the VA approximation in Sec II B 2. To gauge the performance of the VA approximation, we compare results from the VA approximation to those from the 2D description in Sec. III.

### 1. 2D description

The solute is assumed to have constant diffusivity  $D$  in the solvent and is governed by the dimensionless convection-diffusion equation

$$\frac{\partial c}{\partial t} + v_x \frac{\partial c}{\partial x} + v_z \frac{\partial c}{\partial z} = \frac{1}{\text{Pe}} \frac{\partial^2 c}{\partial x^2} + \frac{1}{\epsilon^2 \text{Pe}} \frac{\partial^2 c}{\partial z^2}. \quad (14)$$

Here, the Péclet number  $\text{Pe} = H v_x^*/D\epsilon$  gives the ratio of the lateral diffusive and convective time scales. Similarly,  $\epsilon^2 \text{Pe}$  gives the ratio of the vertical diffusive and convective time scales. Equation (14) is subject to a no-flux condition at the substrate  $z = 0$  and a mass-conservation condition at the interface  $z = h$ :

$$\left. \frac{\partial c}{\partial z} \right|_{z=0} = 0, \quad \left. \frac{\partial c}{\partial z} \right|_{z=h} - \epsilon^2 \frac{\partial h}{\partial x} \left. \frac{\partial c}{\partial x} \right|_{z=h} = \epsilon^2 \text{Pe} E J c|_{z=h}. \quad (15)$$

Specific forms of the mass flux  $J$  and its scale  $J^*$  (which determines  $E$ ) are given in Sec. II C. The 2D description is defined as Eq. (13) coupled with Eq. (14) to describe the film height and full 2D concentration field.

### 2. Vertical-averaging (VA) approximation

When  $\epsilon^2 \text{Pe} \ll 1$ , vertical diffusion is rapid and Eq. (14) may be transformed to describe an approximate, vertically uniform concentration field [10]. To begin, we expand the concentration  $c$  as a perturbation series in powers of  $\epsilon^2 \text{Pe}$ :

$$c(t, x, z) = c_0(t, x, z) + \epsilon^2 \text{Pe} c_1(t, x, z) + O[(\epsilon^2 \text{Pe})^2]. \quad (16)$$

Substituting Eq. (16) into Eq. (14) gives the  $O(1)$  problem

$$\frac{\partial^2 c_0}{\partial z^2} = 0, \quad (17)$$

where we have neglected lateral diffusion because it is an  $O(\epsilon^2)$  effect. Equation (17) is subject to the  $O(1)$  no-flux boundary conditions

$$\left. \frac{\partial c_0}{\partial z} \right|_{z=0} = \left. \frac{\partial c_0}{\partial z} \right|_{z=h} = 0. \quad (18)$$

Equation (17) also requires that  $\epsilon^2 \text{Pe} E \ll 1$ , but given that typically,  $E \ll 1$ , this assumption is valid even if  $\epsilon^2 \text{Pe} \sim 1$ . Equation (17) with boundary conditions (18) reveals that  $c_0$  is independent of  $z$ ; the system is under pseudo-steady-state diffusion at leading order.

The  $O(\epsilon^2 \text{Pe})$  problem is

$$\frac{\partial c_0}{\partial t} + v_{x,0} \frac{\partial c_0}{\partial x} = \frac{1}{\text{Pe}} \frac{\partial^2 c_0}{\partial x^2} + \frac{\partial c_1}{\partial z^2}, \quad (19)$$

where  $v_{x,0}$  is the  $O(1)$  component of the lateral velocity given by

$$v_{x,0} = -\left(\frac{1}{2}z^2 - hz\right) \frac{\partial^3 h}{\partial x^3} - \frac{\partial c_0}{\partial x} z. \quad (20)$$

Equation (19) is subject to the  $O(\epsilon^2 \text{Pe})$  no-flux and mass-conservation conditions

$$\frac{\partial c_1}{\partial z} \Big|_{z=0} = 0, \quad \frac{\partial c_1}{\partial z} \Big|_{z=h} - \frac{1}{\text{Pe}} \frac{\partial h}{\partial x} \frac{\partial c_0}{\partial x} = EJc_0. \quad (21)$$

Applying the averaging operator  $\frac{1}{h} \int_0^h \cdot dz$  to Eq. (19) and using conditions (21) allows one to eliminate  $c_1$  and obtain the governing equation

$$\frac{\partial c_0}{\partial t} + \bar{v}_x \frac{\partial c_0}{\partial x} = \frac{1}{h} \frac{1}{\text{Pe}} \left( h \frac{\partial c_0}{\partial x} \right) + \frac{1}{h} c_0 EJ \quad (22)$$

for  $c_0$ . Here,  $\bar{v}_x$  is the vertically averaged  $O(1)$  lateral velocity given by

$$\bar{v}_x = \frac{1}{h} \int_0^h v_{x,0} dz = \frac{1}{3} h^2 \frac{\partial^3 h}{\partial x^3} - \frac{1}{2} h \frac{\partial c_0}{\partial x}. \quad (23)$$

Equation (22) governs the vertically uniform  $O(1)$  profile  $c_0$  and thus contains no dependence on the vertical coordinate  $z$ . The VA approximation couples Eq. (13) with Eq. (22) to predict the film-height and 1D (vertically uniform) concentration profile. Note that  $\epsilon^2 \text{Pe} \ll 1$  is only a formal assumption to allow asymptotic expansion (16), so it possible that the VA approximation is accurate even outside of this regime (as will be discussed in Sec. III).

### C. Evaporation

As discussed in Sec. I, there are several commonly used evaporation models, three of which we examine in this work. Constant evaporation has the advantage of simplicity and allows one to more easily probe fundamental mechanisms without choosing constitutive models. The one-sided model is also popular for its relative simplicity (compared to the diffusion-limited model) since one only needs to consider transport in the liquid phase. Diffusion-limited evaporation is the most complicated of the three; since gaseous solvent molecules affect the evaporation rate, one must solve coupled transport equations in the liquid and gas phases. In the following sections, we present a brief derivation of each evaporation model and the resulting expressions for the scale  $J^*$  and mass flux  $J$  that appear in Eqs. (13), (15), and (22).

#### 1. Constant evaporation

Constant evaporation is a convenient approximation that is useful for exploring fundamental mechanisms. Under constant evaporation, we simply take the dimensionless mass flux to be  $J = 1$  and  $J^*$  is left arbitrary. Thus, the magnitude of the evaporative term  $EJ$  in Eqs. (13), (15), and (22) is controlled entirely by the constant parameter  $E$ .

#### 2. One-sided evaporation

The one-sided evaporation model gives a constitutive equation for the dimensional mass flux  $J'$  which is derived from kinetic theory and has been modified to account for capillary pressures

[21,30]:

$$\frac{\sqrt{2\pi RT_{\text{sat}}}}{\rho_v} J' = \frac{1}{\rho} p'|_{z'=h'} + \frac{L_m}{T_{\text{sat}}} (T'|_{z'=h'} - T_{\text{sat}}). \quad (24)$$

Here,  $R$  is the ideal gas constant,  $T_{\text{sat}}$  is the saturation temperature of the solvent,  $\rho_v$  is the density of the gaseous solvent, and  $L_m$  is the latent heat of vaporization of the solvent. The dimensional capillary pressure  $p'$  is [after applying scalings (2) to Eq. (8)]

$$p' = -\sigma_0 \frac{\partial^2 h'}{\partial x'^2}. \quad (25)$$

The unknown  $T'$  is the dimensional temperature of the liquid which can be determined analytically under the lubrication approximation.

We introduce the dimensionless temperature  $T = (T' - T_{\text{sat}})/\Delta T$  where  $\Delta T = (T_b - T_{\text{sat}})$ . The quantity  $T_b$  is the substrate temperature so that we enforce  $T' = T_b$  at  $z = 0$ . We take  $T$  to be governed by an energy conservation equation [similar to Eq. (14)], which at leading order is

$$\frac{\partial^2 T}{\partial z^2} = 0. \quad (26)$$

This is subject to the boundary conditions

$$T|_{z=0} = 1, \quad -\frac{\partial T}{\partial z} \Big|_{z=h} = J, \quad (27)$$

where the latter assumes the air above the film has negligible thermal conductivity and the evaporative mass flux  $J$  is scaled by  $J^* = \Delta T k / L_m H$ . In dimensionless form, Eq. (24) reads

$$KJ = \delta p|_{z=h} + T|_{z=h}, \quad (28)$$

where

$$K = \frac{\sqrt{2\pi RT_{\text{sat}}^3} k}{\rho_v L_m^2 H}, \quad \delta = \frac{p^* T_{\text{sat}}}{\rho L_m \Delta T}. \quad (29)$$

Equation (26) is readily solved subject to boundary conditions (27), giving

$$T = 1 - Jz. \quad (30)$$

Substituting Eqs. (8) and (30) into Eq. (28) gives an explicit expression for  $J$ ,

$$J = \frac{1 - \delta \frac{\partial^2 h}{\partial x^2}}{K + h}, \quad (31)$$

in terms of only the film height  $h$ . Because we assume a dilute solute, we have used the solvent properties in this derivation and there is no dependence on the solute concentration  $c$ . In this work, we take  $K = 3.2 \times 10^{-4}$  and  $\delta = 5.9 \times 10^{-7}$ , which are representative of water with a temperature difference of  $\Delta T \approx 3$  K. Note that evaporation is generally more rapid at smaller film heights ( $J \sim 1/h$ ) due to the heated substrate.

### 3. Diffusion-limited evaporation

To derive an explicit expression for the mass flux  $J$  under diffusion-limited evaporation, we must solve for the solvent concentration in the gas phase  $c'_g$ . We define the dimensionless concentration  $c_g = c'_g / c_v$ , where  $c_v$  is the equilibrium vapor pressure of the solvent. Previous studies have shown through scaling arguments that transient terms in the gas-phase convection-diffusion equation are negligible [37], and neglecting convective transport gives Laplace's equation governing  $c_g$ :

$$\frac{\partial^2 c_g}{\partial x^2} + \frac{\partial^2 c_g}{\partial z^2} = 0. \quad (32)$$

One may wish to consider a semi-infinite domain bounded below by the liquid film. A natural boundary condition is then  $c_g \rightarrow 0$  as  $z \rightarrow \infty$ , assuming the ambient vapor pressure is negligible. Unfortunately, such a boundary condition is ill-posed for Laplace's equation in 2D [37]. Instead, we must consider a finite domain [36] of height  $\mathcal{L}$  and apply the boundary condition

$$c_g|_{z=\mathcal{L}} = 0. \quad (33)$$

Appropriate values for the evaporation length parameter  $\mathcal{L}$  are unclear, but we will see that it has little effect on the qualitative behavior of this model. Because the liquid film is thin, its thickness and curvature are  $O(\epsilon)$  effects in the gas phase and we apply Raoult's law at  $z = 0$ :

$$c_g|_{z=0} = f(c) = 1 - \omega_0 c|_{z=h} \quad (34)$$

where  $f(c) = 1 - \omega_0 c|_{z=h}$  is the mole fraction of solvent in the liquid at the interface. Note that the concentration  $c$  is defined in the liquid phase where the film thickness is  $O(1)$ , and thus is evaluated at the liquid-air interface  $z = h$ . The simple form of Eq. (34) is a result of assuming a dilute solute ( $\omega_0 \ll 1$ ) so that we may approximate the liquid's properties as those of the solvent. In this work, we fix  $\omega_0 = 0.1$  since changes in it do not qualitatively affect the results presented in Sec. III. To compute the evaporative mass flux, we note that Fick's law gives

$$J = - \left. \frac{\partial c_g}{\partial z} \right|_{z=0} \quad (35)$$

where the mass flux is scaled by  $J^* = c_v D_g \epsilon / \mathcal{L}$ . Here,  $D_g$  is the diffusivity of the gaseous solvent in air.

Equation (32) subject to boundary conditions (33) and (34) can be solved on the domain  $x \in (0, 2\pi/\alpha)$  and  $z \in (0, \mathcal{L})$  by separation of variables to obtain the flux

$$J = \frac{\bar{f}}{\mathcal{L}} + \sum_{k \neq 0} \tilde{f}_k e^{-\alpha k x} \alpha k \coth(\alpha k \mathcal{L}), \quad (36)$$

where  $\bar{f} = \tilde{f}_0$  is the spatial average of  $f$ ,  $\tilde{f}_k$  is the  $k$ th Fourier coefficient of  $f$ , and  $\alpha$  is the wavenumber of the perturbation described in Sec. III. A detailed derivation of this expression is given in the Appendix. We see that the evaporative flux  $J$  contains a laterally uniform component  $\bar{f}/\mathcal{L}$  that scales linearly with the solvent mole fraction at the interface and inversely with the evaporation length  $\mathcal{L}$ . This term is like constant evaporation, except that it decreases with time as solute builds up and  $\bar{f}$  decreases. We will see in Sec. III that the additional terms in Eq. (36) are self-inhibiting and thus  $J$  is essentially laterally uniform. Therefore, the parameter  $\mathcal{L}$  only affects the magnitude of the evaporative flux and has little effect on its qualitative behavior. In this work, we fix  $\mathcal{L} = 5$ , but results for different  $\mathcal{L}$  are given in the Supplemental Material [49] for reference.

#### D. Thermal Marangoni effects

While we have neglected thermal Marangoni effects in the derivation of this model (see Sec. II A), they warrant a brief discussion because solvent evaporation will induce temperature variations. To account for thermal Marangoni flow in the film, we must solve for the lateral temperature gradient at the interface  $z = h$ . However, the constant and diffusion-limited evaporation models do not include a temperature profile in their derivations, so the temperature profile is not uniquely defined and depends on how one handles heat transfer at the solid substrate [48,50,51]. This is beyond the scope of this work, so we will not discuss thermal Marangoni effects for constant or diffusion-limited evaporation, though they can be appreciable [23,30,38,50–53]. However, for one-sided evaporation, the temperature profile at the interface is given by Eq. (30),

$$T|_{z=h} = 1 - Jh \approx \frac{K}{K+h} \approx \frac{K}{h} \Rightarrow \frac{\partial T|_{z=h}}{\partial x} \approx -\frac{K}{h^2} \frac{\partial h}{\partial x}, \quad (37)$$

TABLE I. Table of important dimensional parameters and their typical values.

Parameter	Definition	Typical values
$H$ (m)	Film thickness	$10^{-5}$ – $10^{-4}$
$\mu$ (Pa s)	Solvent viscosity	$10^{-4}$ – $10^{-3}$
$\sigma_0$ (N/m)	Solvent surface tension	$10^{-2}$ – $10^{-1}$
$D$ (m <sup>2</sup> /s)	Solute diffusivity	$10^{-9}$
$\omega_0$	Solute mass/mole fraction	$10^{-2}$ – $10^{-1}$
$T_{\text{sat}}$ (K)	Saturation temperature	$3 \times 10^2$
$k$ (W/m K)	Thermal conductivity	$10^{-1}$ – $10^0$
$\rho$ (kg/m <sup>3</sup> )	Liquid density	$10^2$ – $10^3$
$\rho_v$ (kg/m <sup>3</sup> )	Vapor density	$10^{-1}$ – $10^0$
$L_m$ (J/kg)	Latent heat of vaporization	$10^5$ – $10^6$

where we have neglected the contribution from capillary pressure since  $\delta \ll 1$ . Equation (37) shows that temperature gradients form over the same  $O(1)$  length scale as film-height gradients. Furthermore,  $K \ll 1$  as discussed in Sec. II C 2, so the dimensionless temperature gradient  $\partial T/\partial x \sim K \ll 1$  is negligible and we do not expect thermal Marangoni effects to be important under one-sided evaporation.

### E. Numerical method and parameter values

There are three dimensionless groups that appear in Eqs. (13), (14), and (22). The first is the Péclet number  $Pe$ , which gives the ratio of the lateral diffusive and convective time scales. The second is the Marangoni number  $Ma = \epsilon^2$ , which gives the ratio of Marangoni forces to capillary forces but also defines the lateral length scale  $L = H/\sqrt{Ma}$ . The Marangoni number appears in the lumped parameter  $\epsilon^2 Pe = MaPe$  that gives the ratio of the vertical diffusive and convective time scales. Note that  $\epsilon^2 Pe$  does not appear in Eq. (22) because vertical diffusion is quasi-steady under the VA approximation. The third is the evaporative number  $E$  which controls the magnitude of the evaporative-flux term  $EJ$ . Typical values of dimensional and dimensionless parameters are given in Tables I and II, respectively. The effects of varying these parameters are explored in Sec. III.

For the 2D description (see Sec. II B 1), Eq. (14) is subject to mass-conservation condition (15) at the moving boundary  $z = h(t, x)$ . To circumvent numerically solving a moving-boundary problem, a coordinate transformation  $(x, z, t) \mapsto (\zeta, \eta, \tau)$  is performed with the relations [54]

$$\eta = \frac{z}{h}, \quad \frac{\partial \zeta}{\partial x} = 1, \quad \frac{\partial \tau}{\partial t} = 1. \quad (38)$$

Here,  $\eta$  is a scaled vertical coordinate,  $\zeta$  is the lateral coordinate, and  $\tau$  is the time coordinate. The interface at  $\eta = 1$  is now constant, but the governing equations become significantly more complex

TABLE II. Important dimensionless parameters and typical values.

Parameter	Definition	Physical meaning	Typical values
$\epsilon$	$H/L, \sqrt{Ma}$	Vertical length/lateral length	$10^{-2}$ – $10^{-1}$
$Ma$	$\Delta\sigma\omega_0/\sigma_0$	Marangoni forces/surface-tension forces	$10^{-3}$ – $10^{-1}$
$E$	$J^*\mu/\rho\sigma_0\epsilon^4$	Evaporative flux/convective flux	$10^{-4}$ – $10^{-2}$
$Pe$	$H\sigma_0\epsilon^2/D\mu$	Diffusion time/convection time	$1$ – $10^6$

with the derivative transformations

$$\frac{\partial}{\partial x} = \frac{\partial}{\partial \zeta} - \frac{\eta}{h} \frac{\partial h}{\partial \zeta} \frac{\partial}{\partial \eta}, \quad \frac{\partial}{\partial z} = \frac{1}{h} \frac{\partial}{\partial \eta}, \quad \frac{\partial}{\partial t} = \frac{\partial}{\partial \tau} - \frac{\eta}{h} \frac{\partial h}{\partial \tau} \frac{\partial}{\partial \eta}. \quad (39)$$

After applying transformation (38) to Eqs. (13) and (14), a pseudospectral method is employed to solve the resulting set of coupled fourth-order nonlinear partial differential equations on the constant domain  $\zeta \in (0, 2\pi/\alpha)$  and  $\eta \in (0, 1)$  [54–56]. To enforce periodicity, the lateral domain is discretized into 64 Fourier modes, while the vertical domain is discretized into 20 Chebyshev polynomials. The equations for the VA approximation contain no dependence on the vertical coordinate, so transformation (38) is not used and the expansion is in Fourier modes only. Note that this is a significant simplification that results in 20 times fewer computational nodes. Time stepping is performed via MATLAB’s solver `ode15i` which is a variable-step, variable-order solver employing backward differentiation. The model and numerical method have been verified by reproducing results for pure film leveling and simple cases of evaporating binary films [6,11,22]. We have also verified that the 2D description and VA approximation are in quantitative agreement at low  $Pe$  (fast vertical diffusion) in Sec. III.

### III. RESULTS AND DISCUSSION

While the VA approximation formally assumes  $\epsilon^2 Pe \ll 1$  (see Sec. II B 2), the actual limits of validity under evaporation have not been established. To examine the performance of the VA approximation, we compare predictions to those from the 2D description (see Sec. II B 1) as the Péclet number  $Pe$  varies. We begin by establishing a metric to compare the VA approximation and 2D description. The initial conditions

$$h(t=0) = 1, \quad c(t=0) = 1 + c_p \cos(\alpha x) \quad (40)$$

represent an initially uniform film thickness and a concentration field with a small lateral perturbation of magnitude  $c_p$ . For all presented results, we take  $c_p = 10^{-2}$  and  $\alpha = 0.3$  since changes to these parameters do not qualitatively influence the results.

Simulations are stopped at time  $t = t_{\max}$ , when the thinnest point of the film reaches  $h_{\min} = 0.1$ , for three reasons. First, we do not include a disjoining pressure in this work that would be required to describe ultrathin films. Second, the transformation described by Eq. (38) becomes stiff, making numerical integration difficult. Third, the diffusion-limited evaporative flux in Eq. (36) decreases in magnitude as solute builds up, reaching 0 when  $c|_{z=h} = \omega_0^{-1}$ . Consequently, with  $\omega_0 = 0.1$ , it can be shown that a spatially uniform film under diffusion-limited evaporation will not decrease below  $h = \omega_0 = 0.1$ .

The perturbation imposed in Eq. (40) causes the film to deform in response to Marangoni flow toward the lateral center of the film ( $x = \pi/\alpha$ ); the perturbation is a depletion of solute in the center of the film, causing a locally high surface tension and Marangoni stresses that drive flow toward the center of the film to form a crest in the film height. However, evaporation of solvent is simultaneously acting to decrease the film height and causes a buildup of solute at the interface. The effects of evaporation on the film height depend on the evaporation model, and the buildup of solute depends on the vertical diffusion time scale  $\epsilon^2 Pe$  (assumed negligible in the VA approximation). Figure 2 shows concentration contours from the 2D description and VA approximation under each evaporation model near parameter values where we first observe discrepancies between the 2D description and VA approximation ( $Pe = 1.7 \times 10^4$ ,  $E = 3 \times 10^{-3}$ , and  $\epsilon = 0.1$ ). Note the differences in the film-height and solute-concentration profiles between the predictions from each approach.

Figures 2(a) and 2(b) show that under constant evaporation, the 2D description predicts a significantly smaller film-height perturbation than the VA approximation. This is due to sharp vertical concentration gradients that form as solute builds up at the interface from solvent evaporation; this will be discussed in Sec. III A. Figures 2(c) and 2(d) show a different trend under one-sided

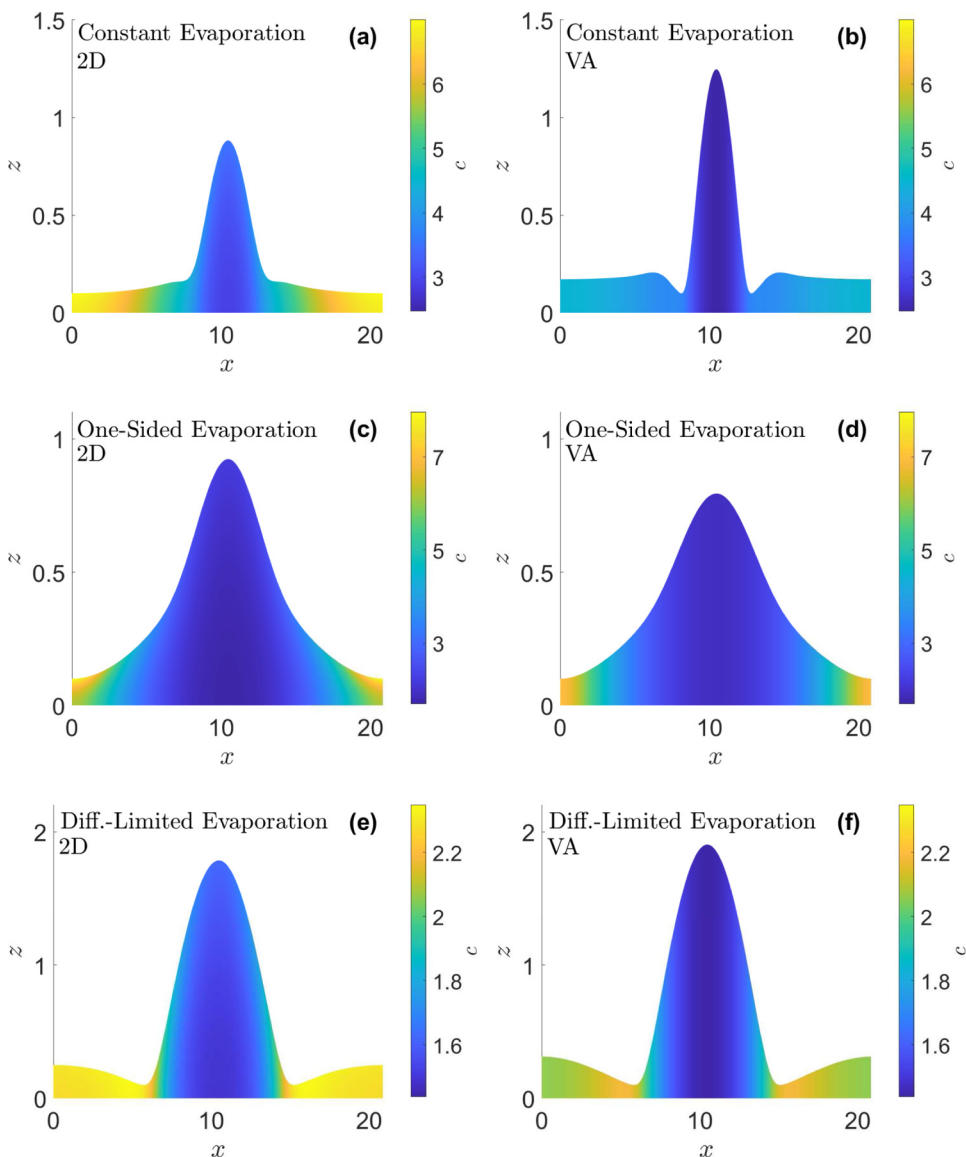


FIG. 2. Concentration contours for  $Pe = 1.7 \times 10^4$ ,  $E = 3 \times 10^{-3}$ , and  $\epsilon = 0.1$  at  $t = t_{\max}$ . Note the qualitative differences in both the film-height and solute concentration profiles. The value of  $Pe$  chosen is near the value where differences between each approach become visible. The corresponding times are (a)  $t_{\max} = 2.56 \times 10^2$ , (b)  $t_{\max} = 2.35 \times 10^2$ , (c)  $t_{\max} = 1.39 \times 10^2$ , (d)  $t_{\max} = 1.41 \times 10^2$ , (e)  $t_{\max} = 7.30 \times 10^2$ , and (f)  $t_{\max} = 6.76 \times 10^2$ . A side-by-side comparison of these profiles is shown in the Supplemental Material [49].

evaporation, where the 2D description predicts a larger film-height perturbation due to the sensitivity of one-sided evaporation to changes in the film height, which will be discussed in Sec. III B. The results under the diffusion-limited evaporation model, depicted in Figs. 2(e) and 2(f), are similar to the case of constant evaporation in Figs. 2(a) and 2(b). This is because the diffusion-limited evaporation model behaves qualitatively like constant evaporation, as will be discussed in Sec. III C. (Figures at larger  $Pe$  are provided in the Supplemental Material [49] where these differences are accentuated.) Figure 2 shows that the size of the film-height perturbation is a useful metric for

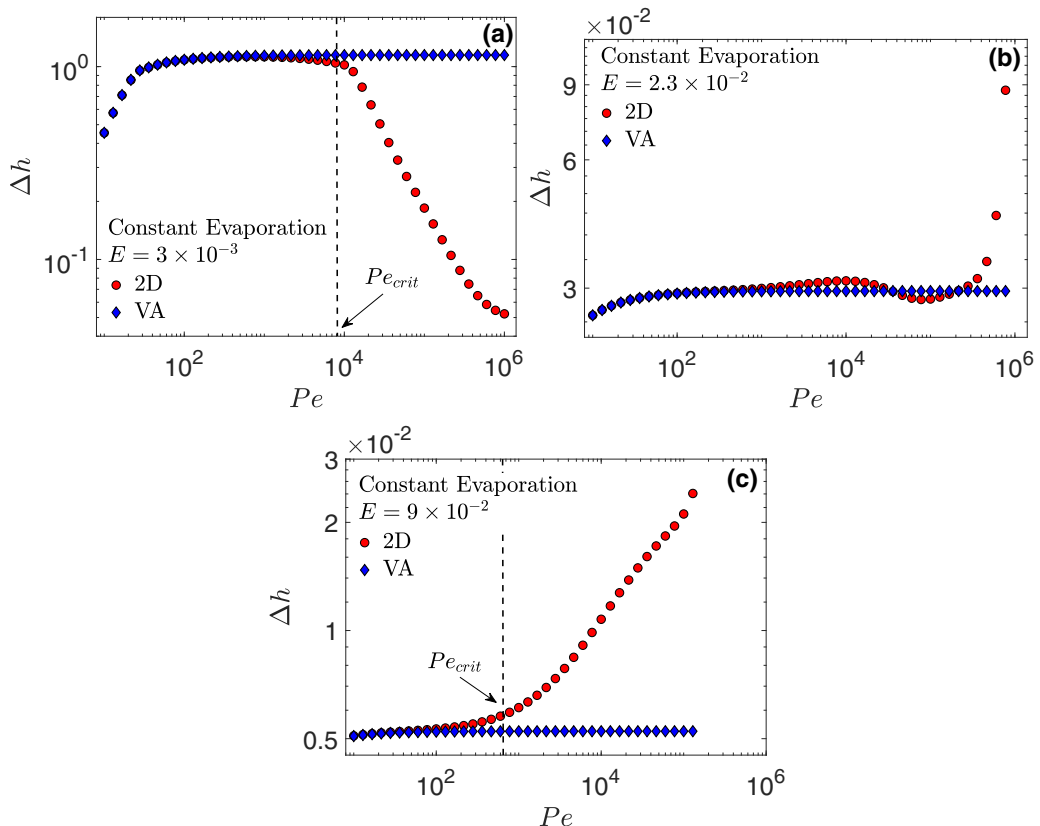


FIG. 3. The height perturbation  $\Delta h$  for (a)  $E = 3 \times 10^{-3}$ , (b)  $E = 2.3 \times 10^{-2}$ , and (c)  $E = 9 \times 10^{-2}$  for varying  $Pe$  and constant evaporation. Note that  $\Delta h$  predicted by the 2D description decreases at large  $Pe$  for small  $E$ , but increases at large  $Pe$  for larger  $E$ .

comparing predictions from the various approaches. At  $t = t_{\max}$ , we denote the peak-to-trough height of the film as  $\Delta h$ .

Figure 2 exemplifies the differences between each modeling approach. From Figs. 2(a) and 2(c), it is clear that the evaporation model significantly affects the predicted film-height profile and solute distribution. Furthermore, Figs. 2(a) and 2(b) show that the VA approximation can lead to drastically different predictions compared to the 2D description. In the following sections we consider each evaporation model in detail and discuss the mechanisms that give rise to the differences between the 2D description and VA approximation.

### A. Constant evaporation

Figures 2(a) and 2(b) show that under constant evaporation with  $E = 3 \times 10^{-3}$ , the 2D description predicts a significantly smaller film-height perturbation  $\Delta h$  than the VA approximation at large  $Pe$ . However, when  $Pe$  is small, one expects rapid vertical diffusion and thus the VA approximation to agree well with the 2D description. To confirm this, Fig. 3(a) shows  $\Delta h$  for a range of  $Pe$  under constant evaporation with  $E = 3 \times 10^{-3}$ . Notably, the 2D description (red circles) and VA approximation (blue diamonds) agree well at small  $Pe$ , but the 2D description predicts a significantly smaller height perturbation  $\Delta h$  than the VA approximation at large  $Pe$  [consistent with Figs. 2(a) and 2(b)]. However, at a larger evaporative number  $E = 9 \times 10^{-2}$  [Fig. 3(c)], the opposite trend occurs, where the 2D description predicts a larger  $\Delta h$ . Consequently, there is a region at intermediate  $E$

where the 2D description transitions from predicting a smaller  $\Delta h$  to a larger  $\Delta h$ , as shown in Fig. 3(b). To understand the trends in Fig. 3, we first explain the behavior at small Pe, then establish precisely what is meant by small or large Pe, and finally elucidate the mechanisms that the VA approximation fails to capture at high Pe.

At sufficiently small Pe, Fig. 3 shows that the 2D description and VA approximation agree well and predict an increasing  $\Delta h$  as Pe increases. Since the evaporative term scales as  $c/h$  in the VA approximation [Eq. (22)], solute buildup from evaporation increases as the film thins. Thus, thinner parts of the film (edges) will develop higher solute concentration than thicker regions (center), exacerbating the perturbation imposed in Eq. (40). The strong Marangoni flows that result can even cause a double-peak film-height profile to develop like that shown in Fig. 2(b). As Pe increases, lateral diffusion slows, so solute concentration perturbations decay less over time and give larger Marangoni stresses and thus larger film-height perturbations for the VA approximation, as shown in Fig. 3.

At large enough Pe, the 2D description and VA approximation no longer agree well. To have a consistent metric for evaluating performance of the VA approximation, we consider the 2D description and VA approximation to not agree well when predictions for  $\Delta h$  differ by more than 10%. The value of Pe at which this first occurs is denoted the critical Péclet number  $Pe_{\text{crit}}$  and is marked in Figs. 3(a) and 3(c). We have not marked  $Pe_{\text{crit}}$  on Fig. 3(b) because the value changes erratically as the system transitions between the two regimes shown in Figs. 3(a) and 3(c). For large Pe ( $Pe > Pe_{\text{crit}}$ ) the 2D description and VA approximation do not agree well, with the 2D description predicting either a smaller or larger  $\Delta h$  depending on the value of  $E$ . Note that the values of  $Pe_{\text{crit}}$  shown in Figs. 3(a) and 3(c),  $Pe_{\text{crit}} \approx 10^4$  and  $Pe_{\text{crit}} \approx 10^3$ , respectively, are larger than the asymptotic assumption  $\epsilon^2 Pe \ll 1$  would suggest ( $Pe_{\text{crit}} \approx 10^2$ ), so the VA approximation is “overperforming.”

The VA approximation is an asymptotic analysis that retains only the leading-order term  $c_0(t, x)$  in Eq. (16). Thus, we may learn what mechanisms it fails to capture by examining the neglected first-order correction  $c_1(t, x, z)$ . By subtracting Eq. (22) from Eq. (19), we obtain a second-order ordinary differential equation for  $c_1$  that can be integrated twice to obtain

$$c_1 - c_1|_{z=0} = \left[ \int_0^z \int_0^{z'} v_{x,0} - \bar{v}_x dz'' dz' \right] \frac{\partial c_0}{\partial x} + \frac{z^2}{2hPe} \frac{\partial h}{\partial x} \frac{\partial c_0}{\partial x} + \frac{z^2 c_0}{2h} EJ, \quad (41)$$

where  $z'$  and  $z''$  are dummy integration variables and  $c_1|_{z=0}$  is an unknown function of  $t$  and  $x$ . This term remains because boundary conditions (21) are insufficient to fully determine  $c_1$ ; rigorously following the asymptotic analysis, we must go to  $O[(\epsilon^2 Pe)^2]$  to determine  $c_1|_{z=0}$ . However, we are only interested in the qualitative behavior of  $c_1$ , so we instead enforce the condition  $\frac{1}{h} \int_0^h c_1 dz = 0$  which implies that  $c_0$  is the vertical average of  $c$  and  $c_1$  is a perturbation around this average. A derivation of  $c_1$  is given in the Appendix.

Figure 3 indicates that the evaporation rate is important in determining when the VA approximation breaks down (i.e.,  $Pe_{\text{crit}}$ ), suggesting that evaporation is likely the dominant term in Eq. (41). Thus, we substitute Eq. (A14) for  $c_1|_{z=0}$  and neglect all terms except evaporation to obtain

$$c_1(t, x, z) \approx \frac{EJhc_0}{2} \left[ \left( \frac{z}{h} \right)^2 - \frac{1}{3} \right]. \quad (42)$$

Note that  $c_1$  is parabolic in  $z$  and decreases as we move away from the interface  $z = h$ . Therefore,  $c_1$  represents vertical solute concentration gradients from evaporation that are not captured by the VA approximation. By examining the magnitude of these gradients, we can determine scaling relations for  $Pe_{\text{crit}}$ .

In the system investigated here, Marangoni flow is the only process through which solute concentration affects film height. The strength of Marangoni flow is determined by the magnitude

of the Marangoni stress

$$\frac{\partial c|_{z=h}}{\partial x} = \frac{\partial c_0}{\partial x} + \epsilon^2 \text{Pe} \frac{\partial c_1|_{z=h}}{\partial x} + O[(\epsilon^2 \text{Pe})^2]. \quad (43)$$

The first-order correction is not captured by the VA approximation, so when this is significant we expect to see film-height profile deviations between the 2D description and VA approximation. Noting that this occurs when  $\text{Pe} \sim \text{Pe}_{\text{crit}}$ , we expect that

$$\frac{\partial c_0}{\partial x} \approx \epsilon^2 \text{Pe}_{\text{crit}} \frac{\partial c_1|_{z=h}}{\partial x} \sim \epsilon^2 \text{Pe}_{\text{crit}} E \frac{\partial}{\partial x} (Jhc_0), \quad (44)$$

where we have used Eq. (42). Under constant evaporation,  $J = 1$  and is constant, but in general  $J = J(x)$  so we retain it in this derivation. Expanding the derivative in Eq. (44) gives

$$\frac{\partial c_0}{\partial x} \sim \epsilon^2 \text{Pe}_{\text{crit}} E \left( \underbrace{Jc_0 \frac{\partial h}{\partial x}}_{(a)} + \underbrace{Jh \frac{\partial c_0}{\partial x}}_{(b)} + \underbrace{hc_0 \frac{\partial J}{\partial x}}_{(c)} \right), \quad (45)$$

which contains contributions from (a) height gradients, (b) lateral concentration gradients, and (c) nonuniform evaporation rates.

By examining each term in Eq. (45), we can understand why the VA approximation breaks down, how  $\text{Pe}_{\text{crit}}$  scales with  $E$ , and if the 2D description will predict a larger or smaller  $\Delta h$  than the VA approximation. Term (a) in Eq. (45) represents a correction for vertical concentration gradients; using boundary conditions (21),

$$EJc_0 \frac{\partial h}{\partial x} \approx \frac{\partial c_1}{\partial z} \Big|_{z=h} \frac{\partial h}{\partial x}, \quad (46)$$

where we have neglected a small diffusive correction. Thus, term (a) in Eq. (45) represents vertical concentration gradients coupling with film-height gradients. Recalling that the solute lowers the surface tension of the liquid, the lateral height ( $\partial h/\partial x$ ) and concentration ( $\partial c_0/\partial x$ ) gradients are opposite in sign (this can be observed in Fig. 2). Since  $\partial c_1/\partial z > 0$  due to evaporation, term (a) in Eq. (45) counteracts Marangoni stresses and if dominant, shows that the 2D description will predict a smaller  $\Delta h$ . Consider Fig. 2(a); if the film were to deform more, then the troughs would descend into regions of lower concentration, which would raise the surface tension. This will pull fluid away from the crests toward the troughs, tending to reverse the deformation. Through this mechanism, vertical concentration gradients can inhibit lateral Marangoni flow. Figure 3(a) shows that the 2D description predicts smaller  $\Delta h$  at lower  $E$ , and thus we expect this mechanism to be dominant at low  $E$  (slow evaporation).

Term (b) in Eq. (45) is always the same sign as the leading-order Marangoni stress  $\partial c_0/\partial x$  and will lead to larger  $\Delta h$  in the 2D description. This term represents a lateral concentration gradient that is localized to the interface. Note the latter of boundary conditions (15) that shows solute buildup at the interface from evaporation ( $\partial c/\partial z$ ) is proportional to the value of the concentration at the interface. Due to the imposed perturbation, the concentration is higher near the edges (troughs) and lower in the center (crest). Thus, concentration will build up locally at the interface faster in the troughs than at the crests, creating a lateral concentration gradient localized to the interface. Through this mechanism, vertical concentration gradients can exacerbate lateral Marangoni flow. Figure 3(c) shows the 2D description predicting larger  $\Delta h$ , and thus we expect this mechanism to be dominant at higher  $E$  (fast evaporation). Term (c) in Eq. (45) is identically zero for constant evaporation but will be discussed in more detail in Sec. III B.

Figure 3(a) shows that at low  $E$ , the 2D description predicts a smaller  $\Delta h$  at high  $\text{Pe}$  and thus we expect term (a) in Eq. (45) is dominant. From this, we can obtain a scaling relation for  $\text{Pe}_{\text{crit}}$  by determining how the film height and concentration scale with  $E$ . To obtain an order-of-magnitude estimate for  $c_0$ , consider the case of a laterally uniform, evaporating film; to conserve mass, we must

have  $c_0 = 1/h$  and so we can expect  $c_0 \sim 1/h$  in a nonuniform system. To obtain an estimate for  $h$ , recall that at the end of the numerical simulations, the minimum value of  $h$  is  $h_{\min} = 0.1$  and thus the maximum value is  $h_{\max} = 0.1 + \Delta h$ . The average of these two values gives

$$h \sim \frac{1}{2}(h_{\min} + h_{\max}) = 0.1 + \frac{1}{2}\Delta h \sim \begin{cases} \text{constant} & \Delta h \ll 0.1 \\ \Delta h & \Delta h \gg 0.1 \end{cases}. \quad (47)$$

Observe in Figs. 3(a) and 3(c) that  $\Delta h \gg 0.1$  at low  $E$  and  $\Delta h \ll 0.1$  at higher  $E$ . Intuitively, very fast evaporation (higher  $E$ ) causes the film to dry out before Marangoni flow can develop a large film-height perturbation, so  $\Delta h$  is smaller at higher  $E$ . Therefore,

$$c_0 \sim \frac{1}{h}, \quad h \sim \begin{cases} \text{constant} & \text{higher } E \\ \Delta h & \text{low } E \end{cases}. \quad (48)$$

Because we are only interested in the scaling with the evaporative number  $E$  and the lateral domain is constant, we take  $\partial h/\partial x \sim \Delta h$  and  $\partial c_0/\partial x \sim \Delta c$ . From Eq. (45), we then have at low  $E$  [using term (a)]

$$\Delta c \sim \epsilon^2 \text{Pe}_{\text{crit}} E \Rightarrow \epsilon^2 \text{Pe}_{\text{crit}} \sim \frac{\Delta c}{E} \quad (\text{low } E), \quad (49)$$

and at higher  $E$  [using term (b)]

$$\Delta c \sim \epsilon^2 \text{Pe}_{\text{crit}} E \Delta c \Rightarrow \epsilon^2 \text{Pe}_{\text{crit}} \sim \frac{1}{E} \quad (\text{higher } E). \quad (50)$$

Relation (50) for higher  $E$  implies that the VA approximation breaks down when  $\epsilon^2 \text{Pe} E \sim \text{constant}$ . The grouping  $\epsilon^2 \text{Pe} E$  represents the relative strengths of vertical diffusion and evaporation, so it is intuitive that this grouping is indicative of the importance of vertical concentration gradients and breakdown of the VA approximation. This is true when evaporation is fast and film-height gradients are unimportant. But when evaporation is slow, there is a coupling between vertical concentration gradients and film-height gradients that leads to a different relation given by Eq. (49). To close relation (49), we must quantify the size of lateral concentration gradients ( $\Delta c$ ) by considering Eqs. (13) and (22).

Note that at the maximum deformation, Marangoni and capillary flow must balance each other, and thus we expect that they scale similarly. From Eqs. (13) and (48), this implies (for low  $E$ )

$$\Delta h^4 \sim \Delta h^2 \Delta c \Rightarrow \Delta c \sim \Delta h^2. \quad (51)$$

For this analysis, we assume that this relation holds at  $t = t_{\max}$  despite not obtaining the maximum deformation. Next, recall that the film-height perturbation develops over time due to Marangoni flow, and thus we balance the time derivative with Marangoni flow in Eq. (13) to obtain

$$\frac{\Delta h}{\Delta t} \sim \Delta h^2 \Delta c \Rightarrow \Delta t \sim \frac{1}{\Delta h \Delta c}. \quad (52)$$

Finally, the evolution of the concentration field is primarily due to evaporation, so we balance the time derivative with evaporation in Eq. (22) to obtain

$$\frac{\Delta c}{\Delta t} \sim \frac{E}{\Delta h^2} \Rightarrow \Delta t \sim \frac{\Delta h^2 \Delta c}{E}. \quad (53)$$

Combining these three relations with relations (49) and (50) gives

$$\epsilon^2 \text{Pe}_{\text{crit}} \sim \begin{cases} E^{-5/7} & \text{low } E \\ E^{-1} & \text{higher } E \end{cases}. \quad (54)$$

To verify Eq. (54), we plot  $\text{Pe}_{\text{crit}}$  for various values of the evaporative number  $E$  obtained from numerical simulations in Fig. 4. Figure 4(a) shows a numerical scaling  $\text{Pe}_{\text{crit}} \sim E^{-0.7}$  at low  $E$  which is close to the analytical scaling  $\text{Pe}_{\text{crit}} \sim E^{-5/7}$  from Eq. (54). Figure 4(b) shows a numerical

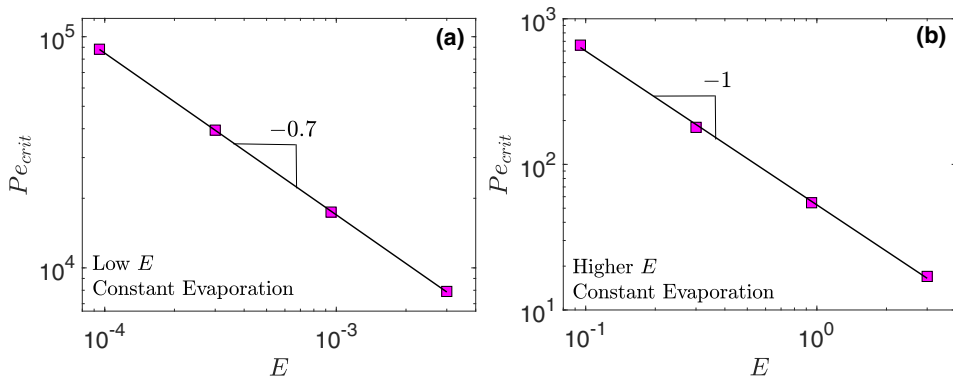


FIG. 4.  $Pe_{crit}$  at various values of  $E$  under constant evaporation for (a) low  $E$  and (b) higher  $E$ . The system transitions between these two scaling regimes at intermediate  $E$  and  $Pe_{crit}$  appears erratic, so these values are not shown.

scaling  $Pe_{crit} \sim E^{-1}$  at higher  $E$  which is exactly the analytical scaling from Eq. (54). However, despite these scaling exponents being similar in magnitude to each other ( $-5/7$  and  $-1$ ), the type of disagreement between the 2D description and VA approximation is qualitatively different as shown in Figs. 3(a) and 3(c) due to the mechanisms discussed above. The weaker scaling at low  $E$  ( $Pe_{crit} \sim E^{-5/7}$ ) is a result of slower evaporation; there is more time for Marangoni flow to develop significant film-height perturbations which decreases the relative importance of evaporation in the system.

When deriving relations (54), we assumed that the vertical concentration gradients from evaporation [reflected in Eq. (42)] lead to the dominant mechanisms that the VA approximation fails to capture. The agreement between relations (54) and the numerical results shown in Fig. 4 shows that the disagreement between the 2D description and VA approximation is indeed due to significant vertical concentration gradients that are important for film evolution. Equation (45) shows the three mechanisms through which vertical concentration gradients influence Marangoni stresses. Term (a) is dominant for slow evaporation and represents direct coupling of vertical concentration gradients with film-height gradients that acts to inhibit Marangoni stresses [see Eq. (46)]. Term (b) is dominant for fast evaporation and represents lateral concentration gradients that develop locally at the interface and exacerbate Marangoni stresses. These two mechanisms cause the discrepancies between the 2D description and the VA approximation for  $Pe > Pe_{crit}$  shown in Fig. 3 and lead to two different relations for  $Pe_{crit}$  given in Eq. (54).

### B. One-sided evaporation

Figures 2(c) and 2(d) show that under one-sided evaporation with  $E = 3 \times 10^{-3}$ , the 2D description predicts a larger film-height perturbation  $\Delta h$  than the VA approximation. This is in contrast to what we observe under constant evaporation in Figs. 2(a) and 2(b) at the same value of  $E$ . Figure 5(a) shows  $\Delta h$  for a range of  $Pe$  and  $E = 3 \times 10^{-3}$  under one-sided evaporation. Like the case of constant evaporation, we observe good agreement between the 2D description and VA approximation at low  $Pe$  ( $Pe < Pe_{crit}$ ), but for  $Pe > Pe_{crit}$  there is no longer good agreement because vertical concentration gradients become significant. However, the deviation between the 2D description and VA approximation in Fig. 5(a) is qualitatively different from that observed under constant evaporation in Fig. 3(a); for all values of  $E$  investigated, the 2D description predicts larger  $\Delta h$  as  $Pe$  increases.

Figure 5(b) shows numerically computed  $Pe_{crit}$  for a large range of  $E$ . At higher  $E$ , we see the same scaling  $Pe_{crit} \sim E^{-1}$  as under constant evaporation in Fig. 4(b), but the behavior is different

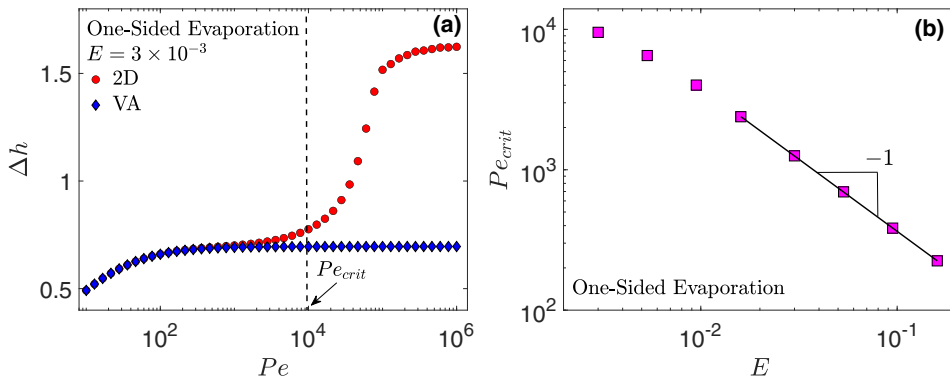


FIG. 5. (a) The height perturbation  $\Delta h$  for  $E = 3 \times 10^{-3}$  and varying  $Pe$  under one-sided evaporation. Note that  $\Delta h$  predicted by the 2D description increases at large  $Pe$ . (b)  $Pe_{\text{crit}}$  at various values of  $E$ .

at low  $E$ ; the erratic transition discussed in Sec. III A is not present, and we instead see a smoother transition with the local slope increasing steadily (becoming less negative) as we decrease  $E$ . Unfortunately, numerical difficulties arising from the large height nonuniformities coupling with the nonuniform evaporation rate have prevented us from obtaining data at lower values of  $E$  than those presented in Fig. 5(b) ( $E < 3 \times 10^{-3}$ ). Nevertheless, the behavior at lower values of  $E$  is qualitatively distinct from that observed under constant evaporation. To understand the mechanisms that cause this, we first briefly discuss the behavior for  $Pe < Pe_{\text{crit}}$  and then revisit Eq. (45) to show how one-sided evaporation causes the 2D description to predict larger  $\Delta h$  even at low  $E$ .

Examining Fig. 5(a), we see that  $\Delta h$  increases as  $Pe$  increases for  $Pe < Pe_{\text{crit}}$ . This is due to the same mechanisms as under constant evaporation; larger  $Pe$  allows larger concentration gradients to persist which causes stronger Marangoni flow and thus larger  $\Delta h$  (see Sec. III A). However, comparing Figs. 3(a) and 5(a), we see that  $\Delta h$  is generally smaller under one-sided evaporation than under constant evaporation for  $Pe < Pe_{\text{crit}}$ . This is because the evaporative flux under one-sided evaporation  $J \sim 1/h$  [Eq. (31)] is faster overall, reducing the time for film deformation and giving smaller  $\Delta h$ . This evaporative flux is also key to explaining the different trend in  $Pe_{\text{crit}}$  in Fig. 5(b). With  $J \sim 1/h$ , evaporation is faster where the film is thinner, so term (c) in Eq. (45) may be significant. Noting that  $\delta \ll 1$  (see Sec. II C 2), we may neglect pressure contributions in Eq. (31) to obtain

$$\frac{\partial J}{\partial x} \approx -\frac{1}{(K+h)^2} \frac{\partial h}{\partial x} \approx -J^2 \frac{\partial h}{\partial x}. \quad (55)$$

One-sided evaporation causes solute to build up more rapidly on the edges of the film (where the film is thin) and more slowly in the center, exacerbating the imposed perturbation at the interface. This causes larger Marangoni stresses that are proportional to the height gradient  $\partial h/\partial x$  as shown in Eq. (55).

Substituting Eq. (55) into relation (45) gives

$$\frac{\partial c_0}{\partial x} \sim \epsilon^2 Pe_{\text{crit}} E \left( \underbrace{Jc_0 \frac{\partial h}{\partial x}}_{(a)} + \underbrace{Jh \frac{\partial c_0}{\partial x}}_{(b)} - \underbrace{c_0 h J^2 \frac{\partial h}{\partial x}}_{(c)} \right). \quad (56)$$

Note that term (a), representing vertical concentration gradients coupling with film-height gradients, and term (c), representing nonuniform solute buildup from a nonuniform evaporative flux, are both proportional to the height gradient  $\partial h/\partial x$  but opposite in sign; the nonuniform buildup of solute caused by nonuniform evaporation [term (c)] causes larger Marangoni stresses that directly

counteract the inhibition of Marangoni stresses by vertical concentration gradients [term (a)]. Furthermore, since  $\delta \ll 1$ ,

$$1 - hJ = 1 - h \frac{1 - \delta p}{K + h} \approx 1 - h \frac{1}{K + h} = \frac{K}{K + h} \approx KJ, \quad (57)$$

so Eq. (56) reduces to

$$\frac{\partial c_0}{\partial x} \sim \epsilon^2 \text{Pe}_{\text{crit}} E \left( \underbrace{KJ^2 c_0 \frac{\partial h}{\partial x}}_{(a)} + \underbrace{Jh \frac{\partial c_0}{\partial x}}_{(b)} \right). \quad (58)$$

As discussed in Sec. III A, the system will be in the low  $E$  regime (where the VA approximation overpredicts  $\Delta h$ ) when film-height gradients are large enough for term (a) to be dominant. In contrast to the case of constant evaporation (Fig. 4), we do not observe a transition to the low  $E$  regime in Fig. 5(b). This is because  $K \ll 1$ , so film-height gradients are not large enough to make term (a) dominant and the system remains in the higher  $E$  regime where term (b), representing lateral concentration gradients that develop locally at the interface, is dominant. Nevertheless, we can still derive scaling relations in both the low  $E$  and higher  $E$  regimes.

Analogous to the case of constant evaporation in Sec. III A, term (b) in Eq. (58) is dominant at higher  $E$  since  $\Delta h$  is small and we expect  $\text{Pe}_{\text{crit}} \sim E^{-1}$  as shown in Fig. 5(b). However, the case for low  $E$  is different, and we must reconsider how  $h$  and  $c_0$  scale with  $E$ . For mass conservation, we have  $c_0 \sim 1/h$  and from Eq. (31),  $J \sim 1/h$  since  $K, \delta \ll 1$ . Taking  $\partial h/\partial x \sim \Delta h$  and  $\partial c_0/\partial x \sim \Delta c$  as in Sec. III A, we have from Eq. (45)

$$\Delta c \sim \epsilon^2 \text{Pe}_{\text{crit}} \frac{E}{\Delta h^2} \Rightarrow \epsilon^2 \text{Pe}_{\text{crit}} \sim \frac{\Delta c \Delta h^2}{E}. \quad (59)$$

The scaling relation for  $h$  is given by Eq. (48), and relations (51) and (52) hold regardless of the evaporation model. However, the relation obtained from Eq. (22) is different due to a different scaling for  $J$ :

$$\frac{\Delta c}{\Delta t} \sim \frac{E}{\Delta h^3} \Rightarrow \Delta t \sim \frac{\Delta h^3 \Delta c}{E}. \quad (60)$$

Combining this with relations (51), (52), and (59) gives  $\epsilon^2 \text{Pe}_{\text{crit}} \sim E^{-1/2}$ . We thus have the relations

$$\epsilon^2 \text{Pe}_{\text{crit}} \sim \begin{cases} E^{-1/2} & \text{low } E \\ E^{-1} & \text{higher } E \end{cases}. \quad (61)$$

While we are unable to verify the scaling at low  $E$  numerically, it reveals that  $\text{Pe}_{\text{crit}}$  has an even weaker dependence on  $E$  under one-sided evaporation ( $\text{Pe}_{\text{crit}} \sim E^{-1/2}$ ) than under constant evaporation ( $\text{Pe}_{\text{crit}} \sim E^{-5/7}$ ). This is because, as discussed above, the nonuniform buildup of solute from one-sided evaporation counteracts the effects of vertical concentration gradients coupling with film-height gradients. Consequently, at very low  $E$ , we expect the VA approximation to perform well at higher  $\text{Pe}$  under one-sided evaporation ( $\text{Pe}_{\text{crit}} \sim E^{-1/2}$ ) compared to constant evaporation ( $\text{Pe}_{\text{crit}} \sim E^{-5/7}$ ). However, at higher  $E$ , the one-sided and constant evaporation models have the same dominant mechanism (lateral solute concentration gradients developing locally at the interface) and thus have identical scaling relations  $\text{Pe}_{\text{crit}} \sim E^{-1}$ .

### C. Diffusion-limited evaporation

Examining Figs. 2(e) and 2(f), we note that the profiles predicted by both the 2D description and VA approximation under diffusion-limited evaporation are qualitatively similar to those under constant evaporation shown in Figs. 2(a) and 2(b). However, diffusion-limited evaporation results in larger film-height perturbations. Figures 6(a) and 6(b) show  $\Delta h$  for a range of  $\text{Pe}$  and two different values of  $E$  under diffusion-limited evaporation. Comparing Fig. 6(a) to Fig. 3(a), we indeed see

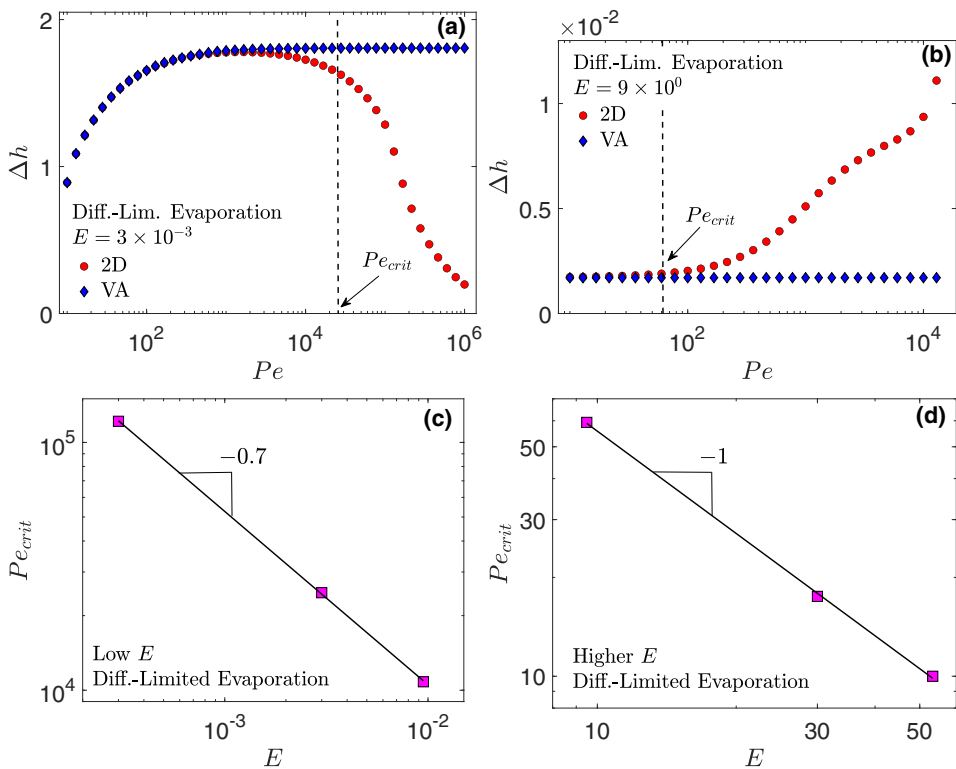


FIG. 6. The height perturbation  $\Delta h$  for (a)  $E = 3 \times 10^{-3}$  and (b)  $E = 3 \times 10^{-2}$  for varying  $Pe$ , and  $Pe_{crit}$  at various values of  $E$  under diffusion-limited evaporation for (c) low  $E$  and (d) higher  $E$ . Note the similarities to constant evaporation in Figs. 3 and 4.

that the height perturbation  $\Delta h$  under diffusion-limited evaporation is larger than that under constant evaporation. This is because the evaporation rate  $EJ$  is generally slower under diffusion-limited evaporation; as solute builds up, the evaporative flux  $J$  decreases, giving a generally slower evaporation rate at a fixed value of  $E$  (compared to constant evaporation). Thus, Marangoni flow has more time to develop film-height nonuniformities which results in larger  $\Delta h$ .

Figures 6(a) and 6(b) show that  $\Delta h$  has the same qualitative behavior as under constant evaporation shown in Fig. 3. Figures 6(c) and 6(d) show  $Pe_{crit}$  as a function of  $E$  for the cases of low and higher  $E$  where we see that the numerical scaling relations are identical to the case of constant evaporation shown in Fig. 4. These similarities indicate that diffusion-limited evaporation qualitatively behaves like constant evaporation; observe that the evaporative flux given by Eq. (36) is smaller where the solute concentration is higher because less solvent is available at the interface. This inhibits nonuniform solute buildup because any regions of high solute concentration will experience slower evaporation, which inhibits further solute buildup. Comparing Figs. 2(a) and 2(e), we indeed see that diffusion-limited evaporation results in a more uniform concentration profile (note the color bar scales). Thus, diffusion-limited evaporation given by Eq. (36) essentially becomes a spatially uniform evaporative flux  $J \approx \bar{f}/\mathcal{L}$  that decreases with time as solute concentration increases.

The time-dependence of this uniform evaporation rate does not affect the scaling relations for  $Pe_{crit}$ , since from Eqs. (34) and (36), we have

$$\frac{\partial J}{\partial x} \approx \frac{1}{\mathcal{L}} \frac{\partial \bar{f}}{\partial x} = -\frac{\omega_0}{\mathcal{L}} \frac{\partial c|_{z=h}}{\partial x} \ll 1, \quad (62)$$

since  $\omega_0 \ll 1$  and  $c \sim O(1)$  [as shown in Fig. 2(e)]. Thus, under diffusion-limited evaporation, we expect the same scaling relations for  $Pe_{\text{crit}}$  that we saw for constant evaporation [given by Eq. (44)]. However, note that the transition from low  $E$  [Fig. 6(c)] to higher  $E$  [Fig. 6(d)] occurs at a higher value of  $E$  than under constant evaporation [Figs. 4(a) and 4(b)]. This is because, as discussed earlier, diffusion-limited evaporation results in a more uniform concentration profile. This inhibits the mechanisms that are dominant in the higher  $E$  regime since they rely on evaporation forming large lateral concentration gradients (see Sec. III A). Thus, the system remains in the low  $E$  regime, where the dominant mechanism instead depends on film-height gradients (see Sec. III A), for a larger range of  $E$ .

#### IV. CONCLUSIONS

We have evaluated the performance of the VA approximation under three common evaporation models—constant, one-sided, and diffusion-limited—for an evaporating, two-component thin liquid film. To focus on solutal Marangoni flow, we neglected any thermal effects induced by evaporation of solvent (discussed in Sec. II D). The model assumes the liquid is Newtonian with constant viscosity and density, that the solute is dilute, and that the Marangoni number is small. The VA approximation offers a desirable simplicity when modeling multicomponent systems that has led to its use in a wealth of previous studies. However, until this work, its limits of validity had not been systemically explored under evaporation. While the VA approximation is formally presented with the assumption  $\epsilon^2 Pe \ll 1$  (for rapid vertical diffusion) [10], it was found that the necessary assumption is instead  $Pe < Pe_{\text{crit}}$ , where  $Pe_{\text{crit}}$  is a critical Péclet number reflecting the physical mechanisms underlying film evolution that the VA approximation fails to capture.

It was shown that  $Pe_{\text{crit}}$  depends on the evaporation model, and scaling relations were derived in Sec. III A and Sec. III B to elucidate how  $Pe_{\text{crit}}$  scales with the evaporative number  $E$  under each evaporation model. Notably, it was found that, often,  $\epsilon^2 Pe_{\text{crit}} \gg 1$ , and so the VA approximation “overperforms” its formal assumption  $\epsilon^2 Pe \ll 1$  by several orders of magnitude. However, when  $Pe > Pe_{\text{crit}}$ , vertical concentration gradients from evaporation become important and it was found that the chosen evaporation model greatly influences system behavior. Vertical concentration gradients from evaporation directly inhibit film deformation if the film-height nonuniformity is large enough, but for sufficiently fast evaporation, large lateral concentration gradients form locally at the interface and cause larger film-height nonuniformities (see Sec. III A). These lateral concentration gradients near the interface become particularly pronounced under one-sided evaporation, exacerbating Marangoni stresses and causing larger film-height nonuniformities (see Sec. III B). In contrast, diffusion-limited evaporation was found to be qualitatively similar to the much simpler case of constant evaporation because any nonuniformity in the evaporative flux is self-inhibiting (see Sec. III C).

While the VA approximation overperforms relative to its formal assumptions, one must be cognizant of the value of  $\epsilon^2 Pe$  when employing the VA approximation, and also how the chosen evaporation model may qualitatively influence results. If the VA approximation is used outside of its range of validity, film-height and solute-concentration contours should be interpreted with caution. For systems at large  $Pe$ , it is best to use a 2D description for species distribution and it is crucial to accurately characterize evaporation. Scaling relations (54) and (61) provide guidelines for what a large value of  $Pe$  is.

#### ACKNOWLEDGMENTS

This work was supported by the Industrial Partnership for Research in Interfacial and Materials Engineering of the University of Minnesota. We also acknowledge partial support through a fellowship awarded to C.L. by the PPG Foundation.

## APPENDIX

## 1. Solution of Laplace's equation

We wish to solve Laplace's equation  $\nabla^2 u = 0$  for the function  $u$  on the rectangular domain  $(x, z) \in [0, L_x] \times [0, L_z]$  with periodic conditions in  $x$  and the following conditions in  $z$ :

$$u|_{z=0} = f(x), \quad u|_{z=L_z} = 0. \quad (\text{A1})$$

Decomposing  $u = \phi(x)\Psi(z)$  and substituting into Laplace's equation yields the two ordinary differential equations

$$\frac{\partial^2 \phi}{\partial x^2} + \lambda^2 \phi = 0, \quad \frac{\partial^2 \Psi}{\partial z^2} - \lambda^2 \Psi = 0, \quad (\text{A2})$$

where  $\lambda$  is an undetermined (eigen)value. Considering the periodic conditions in  $x$ , we must have  $\sqrt{\lambda} = 2\pi k/L_x$  for  $k \in \mathbb{Z}$  and solutions are of the form

$$\phi(x) = Ae^{\frac{2\pi k}{L_x}ix}, \quad \Psi(z) = Be^{\frac{2\pi k}{L_x}z} + Ce^{-\frac{2\pi k}{L_x}z}. \quad (\text{A3})$$

Requiring that  $u|_{z=L_z} = 0$  gives the relation  $B = -Ce^{-4\pi k\ell}$  where  $\ell = L_z/L_x$ . The function  $u$  is thus of the form

$$u(x, z) = \sum_k A_k e^{\frac{2\pi k}{L_x}ix} (e^{-\frac{2\pi k}{L_x}z} - e^{\frac{2\pi k}{L_x}z - 4\pi k\ell}), \quad (\text{A4})$$

where  $\{A_k\}_{k \in \mathbb{Z}}$  are constants. At  $z = 0$ , we have  $u(x, z = 0) = f(x)$  and thus

$$f(x) = \sum_k A_k e^{\frac{2\pi k}{L_x}ix} (1 - e^{-4\pi k\ell}). \quad (\text{A5})$$

Multiplying by the basis function  $e^{-\frac{2\pi m}{L_x}ix}$  and applying the operator  $\frac{1}{L_x} \int_0^{L_x} \cdot dx$  gives expressions for the unknown constants:

$$A_m = \frac{1}{L_x} \frac{1}{1 - e^{-4\pi m\ell}} \int_0^{L_x} f(x) e^{-\frac{2\pi m}{L_x}ix} dx = \frac{\tilde{f}_m}{1 - e^{-4\pi m\ell}}, \quad (\text{A6})$$

where  $\tilde{f}_m$  is the  $m$ th Fourier coefficient of  $f$ .

The flux at the interface  $z = 0$  is obtained by Fick's law:

$$J = -\left. \frac{\partial u}{\partial z} \right|_{z=0} = \sum_k \frac{2\pi k}{L_x} A_k e^{-\frac{2\pi k}{L_x}ix} (1 + e^{-4\pi k\ell}) = \frac{2\pi}{L_x} \sum_k \tilde{f}_k e^{-\frac{2\pi k}{L_x}ix} k \coth(2\pi k\ell). \quad (\text{A7})$$

The value for  $k = 0$  must be taken in a limiting sense. It is, however, instructive to separate it from the sum to see

$$J = \frac{\bar{f}}{L_z} + \frac{2\pi}{L_x} \sum_{k \neq 0} \tilde{f}_k e^{-\frac{2\pi k}{L_x}ix} k \coth(2\pi k\ell), \quad (\text{A8})$$

where  $\bar{f} = \tilde{f}_0$  is the average of  $f$  over  $(0, L_x)$ . Taking  $L_x = 2\pi/\alpha$  and  $L_z = \mathcal{L}$  as in Sec. II C, the solution reads

$$J = \frac{\bar{f}}{\mathcal{L}} + \sum_{k \neq 0} \tilde{f}_k e^{-\alpha k ix} \alpha k \coth(\alpha k \mathcal{L}), \quad (\text{A9})$$

which is Eq. (36). One may recognize this solution as a discrete Fourier transform, and thus truncations of it can be efficiently computed by FFT algorithms.

## 2. Higher-order terms in VA approximation

In the VA approximation, one expands the concentration field in a perturbation series given by Eq. (16). Using this, one derives governing Eq. (19) and averages to obtain Eq. (22). By subtracting these two equations, we obtain

$$\frac{\partial^2 c_1}{\partial z^2} = (v_{x,0} - \bar{v}_x) \frac{\partial c_0}{\partial x} + \frac{1}{h\text{Pe}} \frac{\partial h}{\partial x} \frac{\partial c_0}{\partial x} + \frac{c_0}{h} EJ, \quad (\text{A10})$$

which gives  $c_1$  purely in terms of  $c_0$  and  $h$ , and this can be integrated twice to obtain

$$c_1 - c_1|_{z=0} = \left[ \int_0^z \int_0^{z'} v_{x,0} - \bar{v}_x dz'' dz' \right] \frac{\partial c_0}{\partial x} + \frac{z^2}{2h\text{Pe}} \frac{\partial h}{\partial x} \frac{\partial c_0}{\partial x} + \frac{z^2 c_0}{2h} EJ, \quad (\text{A11})$$

$$\int_0^z \int_0^{z'} v_{x,0} - \bar{v}_x dz'' dz' = -\frac{1}{6} \left( \frac{1}{4} z^4 - h z^3 + h^2 z^2 \right) \frac{\partial}{\partial x} \left[ h x - \frac{1}{2} \left( \frac{1}{3} z^3 - \frac{1}{2} h z^2 \right) \right] \frac{\partial c_0}{\partial x}. \quad (\text{A12})$$

The boundary conditions for  $c_1$  given by Eqs. (21) are insufficient to fully determine  $c_1$ , so we enforce the condition

$$\frac{1}{h} \int_0^h c_1 dz = 0. \quad (\text{A13})$$

This implies that  $c_0$  is the vertical average of  $c$  and that  $c_1$  gives a perturbation around this average. We then have

$$c_1|_{z=0} = - \left[ \frac{1}{h} \int_0^h \int_0^z \int_0^{z'} v_{x,0} - \bar{v}_x dz'' dz' dz \right] \frac{\partial c_0}{\partial x} - \frac{h}{6\text{Pe}} \frac{\partial h}{\partial x} \frac{\partial c_0}{\partial x} - \frac{h c_0}{6} EJ, \quad (\text{A14})$$

$$\frac{1}{h} \int_0^h \int_0^z \int_0^{z'} v_{x,0} - \bar{v}_x dz'' dz' dz = -\frac{1}{45} h^4 \frac{\partial^3 h}{\partial x^3} + \frac{1}{24} h^3 \frac{\partial c_0}{\partial x}. \quad (\text{A15})$$

To evaluate the magnitude of Marangoni stresses, we require the concentration at the interface  $c_1|_{z=h}$ . With the above, this is given by

$$c_1|_{z=h} = \frac{1}{72} \left( -\frac{7}{5} h^4 \frac{\partial^3 h}{\partial x^3} + h^3 \frac{\partial c_0}{\partial x} \right) \frac{\partial c_0}{\partial x} + \frac{h}{3\text{Pe}} \frac{\partial h}{\partial x} \frac{\partial c_0}{\partial x} + \frac{h c_0}{3} EJ. \quad (\text{A16})$$

- 
- [1] J. R. A. Pearson, On convection cells induced by surface tension, *J. Fluid Mech.* **4**, 489 (1958).  
 [2] K. B. Sutton, C. B. Clemons, K. L. Kreider, J. P. Wilber, and G. W. Young, Surface nonuniformities in latex paints due to evaporative mechanisms, *AIChE J.* **64**, 1841 (2018).  
 [3] M. H. Eres, D. E. Weidner, and L. W. Schwartz, Three-dimensional direct numerical simulation of surface-tension-gradient effects on the leveling of an evaporating multicomponent fluid, *Langmuir* **15**, 1859 (1999).  
 [4] P. Koliopoulos, K. S. Jochem, R. K. Lade Jr., L. F. Francis, and S. Kumar, Capillary flow with evaporation in open rectangular microchannels, *Langmuir* **35**, 8131 (2019).  
 [5] R. V. Craster and O. K. Matar, Dynamics and stability of thin liquid films, *Rev. Mod. Phys.* **81**, 1131 (2009).  
 [6] A. Oron, S. H. Davis, and S. G. Bankoff, Long-scale evolution of thin liquid films, *Rev. Mod. Phys.* **69**, 931 (1997).  
 [7] M. Schulz and J. L. Keddie, A critical and quantitative review of the stratification of particles during the drying of colloidal films, *Soft Matter* **14**, 6181 (2018).  
 [8] R. Horiuchi, W. J. Suszynski, and M. S. Carvalho, Simultaneous multilayer coating of water-based and alcohol-based solutions, *J. Coat. Technol. Res.* **12**, 819 (2015).  
 [9] M. Dey, F. Doumenc, and B. Guerrier, Numerical simulation of dip-coating in the evaporative regime, *Eur. Phys. J. E* **39**, 19 (2016).

- [10] O. E. Jensen and J. B. Grotberg, The spreading of heat or soluble surfactant along a thin liquid film, *Phys. Fluids* **5**, 58 (1993).
- [11] C. Larsson and S. Kumar, Nonuniformities in miscible two-layer two-component thin liquid films, *Phys. Rev. Fluids* **6**, 034004 (2021).
- [12] T. Pham, X. Cheng, and S. Kumar, Drying of multicomponent thin films on substrates with topography, *J. Polym. Sci. Part B: Polym. Phys.* **55**, 1681 (2017).
- [13] T. Pham and S. Kumar, Imbibition and evaporation of droplets of colloidal suspensions on permeable substrates, *Phys. Rev. Fluids* **4**, 034004 (2019).
- [14] J. Eggers and L. M. Pismen, Nonlocal description of evaporating drops, *Phys. Fluids* **22**, 112101 (2010).
- [15] R. G. Larson, Transport and deposition patterns in drying sessile droplets, *AIChE J.* **60**, 1538 (2014).
- [16] S. D. Howison, J. A. Moriarty, J. R. Ockendon, E. L. Terrill, and S. K. Wilson, A mathematical model for drying paint layers, *J. Eng. Math.* **32**, 377 (1997).
- [17] C. Parrish and S. Kumar, Simultaneous liquid flow and drying on rotating cylinders, *Phys. Rev. Fluids* **5**, 034001 (2020).
- [18] L. Espín and S. Kumar, Sagging of evaporating droplets of colloidal suspensions on inclined substrates, *Langmuir* **30**, 11966 (2014).
- [19] M. R. Moore, D. Vella, and J. M. Oliver, The nascent coffee ring: How solute diffusion counters advection, *J. Fluid Mech.* **920**, A54 (2021).
- [20] H. J. Palmer, The hydrodynamic stability of rapidly evaporating liquids at reduced pressure, *J. Fluid Mech.* **75**, 487 (1976).
- [21] J. P. Burelbach, S. G. Bankoff, and S. H. Davis, Nonlinear stability of evaporating/condensing liquid films, *J. Fluid Mech.* **195**, 463 (1988).
- [22] S. K. Serpetsi and S. G. Yiantsios, Stability characteristics of solutocapillary Marangoni motion in evaporating thin films, *Phys. Fluids* **24**, 122104 (2012).
- [23] S. G. Yiantsios and B. G. Higgins, Marangoni flows during drying of colloidal films, *Phys. Fluids* **18**, 082103 (2006).
- [24] S. G. Yiantsios and B. G. Higgins, A mechanism of Marangoni instability in evaporating thin liquid films due to soluble surfactant, *Phys. Fluids* **22**, 022102 (2010).
- [25] S. G. Yiantsios, S. K. Serpetsi, F. Doumenc, and B. Guerrier, Surface deformation and film corrugation during drying of polymer solutions induced by Marangoni phenomena, *Int. J. Heat Mass Transf.* **89**, 1083 (2015).
- [26] M. Rodríguez-Hakim, J. M. Barakat, X. Shi, E. S. G. Shaqfeh, and G. G. Fuller, Evaporation-driven solutocapillary flow of thin liquid films over curved substrates, *Phys. Rev. Fluids* **4**, 034002 (2019).
- [27] A. F. Routh and W. B. Zimmerman, Distribution of particles during solvent evaporation from films, *Chem. Eng. Sci.* **59**, 2961 (2004).
- [28] C. M. Cardinal, Y. D. Jung, K. H. Ahn, and L. F. Francis, Drying regime maps for particulate coatings, *AIChE J.* **56**, 2769 (2010).
- [29] C. Sotke, V. S. Ajaev, and P. Stephan, Dynamics of volatile liquid droplets on heated surfaces: Theory versus experiment, *J. Fluid Mech.* **610**, 343 (2008).
- [30] V. S. Ajaev, Spreading of thin volatile liquid droplets on uniformly heated surfaces, *J. Fluid Mech.* **528**, 279 (1999).
- [31] T. Pham and S. Kumar, Drying of droplets of colloidal suspensions on rough substrates, *Langmuir* **33**, 10061 (2017).
- [32] K. L. Maki and S. Kumar, Fast evaporation of spreading droplets of colloidal suspensions, *Langmuir* **27**, 11347 (2011).
- [33] G. Karapetsas, K. C. Sahu, and O. K. Matar, Evaporation of sessile droplets laden with particles and insoluble surfactants, *Langmuir* **32**, 6871 (2016).
- [34] D. P. Sheetz, Formation of films by drying of latex, *J. Appl. Polym. Sci.* **9**, 3759 (1965).
- [35] A. F. Routh, Drying of thin colloidal films, *Rep. Prog. Phys.* **76**, 046603 (2013).
- [36] C. Loussert, F. Doumenc, J. B. Salmon, V. S. Nikolayev, and B. Guerrier, Role of vapor mass transfer in flow coating of colloidal dispersions in the evaporative regime, *Langmuir* **33**, 14078 (2017).

- [37] E. Sultan, A. Boudaoud, and M. B. Amar, Evaporation of a thin film: Diffusion of the vapour and Marangoni instabilities, *J. Fluid Mech.* **543**, 183 (2005).
- [38] B. Sobac, P. Colinet, and L. Pauchard, Influence of Bénard-Marangoni instability on the morphology of drying colloidal films, *Soft Matter* **15**, 2381 (2019).
- [39] R. D. Deegan, O. Bakajin, T. F. Dupont, G. Huber, S. R. Nagel, and T. A. Witten, Capillary flow as the cause of ring stains from dried liquid drops, *Nature (London)* **389**, 827 (1997).
- [40] R. D. Deegan, O. Bakajin, T. F. Dupont, G. Huber, S. R. Nagel, and T. A. Witten, Contact line deposits in an evaporating drop, *Phys. Rev. E* **62**, 756 (2000).
- [41] H. Hu and R. G. Larson, Evaporation of a sessile droplet on a substrate, *J. Phys. Chem. B* **106**, 1334 (2002).
- [42] C. Diddens, J. G. M. Kuerten, C. W. M. van der Geld, and H. M. A. Wijshoff, Modeling the evaporation of sessile multi-component droplets, *J. Colloid Interface Sci.* **487**, 426 (2017).
- [43] P. J. Sáenz, A. W. Wray, Z. Che, O. K. Matar, P. Valluri, J. Kim, and K. Sefiane, Dynamics and universal scaling law in geometrically-controlled sessile drop evaporation, *Nat. Commun.* **8**, 14783 (2017).
- [44] B. Sobac, P. Talbot, B. Haut, A. Rednikov, and P. Colinet, A comprehensive analysis of the evaporation of a liquid spherical drop, *J. Colloid Interface Sci.* **438**, 306 (2015).
- [45] P. Talbot, B. Sobac, A. Rednikov, P. Colinet, and B. Haut, Thermal transients during the evaporation of a spherical liquid drop, *Int. J. Heat Mass Transf.* **97**, 803 (2016).
- [46] B. Sobac, Z. Larbi, P. Colinet, and B. Haut, Mathematical modeling of the drying of a spherical colloidal drop, *Colloids Surf., A* **576**, 110 (2019).
- [47] C. Poulard, O. Bénichou, and A. M. Cazabat, Freely receding evaporating droplets, *Langmuir* **19**, 8828 (2003).
- [48] N. Murisic and L. Kondic, On evaporation of sessile drops with moving contact lines, *J. Fluid Mech.* **679**, 219 (2011).
- [49] See Supplemental Material at <http://link.aps.org/supplemental/10.1103/PhysRevFluids.7.094002> for additional figures.
- [50] W. D. Ristenpart, P. G. Kim, C. Domingues, J. Wan, and H. A. Stone, Influence of Substrate Conductivity on Circulation Reversal in Evaporating Drops, *Phys. Rev. Lett.* **99**, 234502 (2007).
- [51] H. Hu and R. G. Larson, Marangoni effect reverses coffee-ring depositions, *J. Phys. Chem. B* **110**, 7090 (2006).
- [52] M. Bestehorn and I. D. Borcia, Thin film lubrication dynamics of a binary mixture: Example of an oscillatory instability, *Phys. Fluids* **22**, 104102 (2010).
- [53] L. E. Scriven and C. V. Sterlring, On cellular convection driven by surface-tension gradients: Effects of mean surface tension and surface viscosity, *J. Fluid Mech.* **19**, 321 (1964).
- [54] M. Dey, A. S. Vivek, H. N. Dixit, A. Richhariya, and J. J. Feng, A model of tear-film breakup with continuous mucin concentration and viscosity profiles, *J. Fluid Mech.* **858**, 352 (2019).
- [55] J. P. Boyd, *Chebyshev and Fourier Spectral Methods: Second Revised Edition* (Courier Corporation, North Chelmsford, MA, 2001)
- [56] L. N. Trefethen, *Spectral Methods in MATLAB* (SIAM, Philadelphia, PA, 2000).